water

MDPI

Article

Study on Pressure Pulsation and Force Characteristics of Kaplan Turbine

Chengming Liu [1], Tao Chen [2], Wenzhe Kang [1], Jianjun Kang [2], Lingjiu Zhou [1], Ran Tao[1] and Zhengwei Wang [3,*]

[1] College of Water Resources and Civil Engineering, China Agricultural University, Beijing 100083, China; lamous3006@163.com (C.L.); kwz@cau.edu.cn (W.K.); zlj@cau.edu.cn (L.Z.); randytao@cau.edu.cn (R.T.)
[2] Guangxi Datengxia Gorge Water Conservancy Development Co., Ltd., Guiping 537226, China; total_00@163.com (T.C.); kangjianjun2013@163.com (J.K.)
[3] State Key Laboratory of Hydroscience and Engineering, Department of Energy and Power Engineering, Tsinghua University, Beijing 100084, China
* Correspondence: wzw@mail.tsinghua.edu.cn

Abstract: With the continuous increase in the size and power generation of turbines, the operational characteristics of turbines under off-design conditions are gradually receiving attention. In this paper, the Reynolds time-averaged method (RANS) is applied to the unsteady calculation of three different flow rate of a large Kaplan turbine under three heads: high head, rated head and low head. The focus is on the internal flow pattern of the turbine and the hydraulic excitation characteristics under low flow conditions. The unsteady characteristics of pressure pulsation, axial force of runner, radial force of runner and hydraulic torques along blade shank (τ_b) for six blades are analyzed. The results show that the pressure pulsation in the vaneless space is larger under low flow conditions, and frequencies of 0.33–1 fn (fn is the rotating frequency of the runner) can be observed at monitoring points at different heights in the vaneless space. The analysis of the flow field under low flow conditions reveals the presence of larger scale vortices in the vaneless space. The position and intensity of vortices fluctuate periodically and cause larger amplitude pressure fluctuations. The frequency of 0.33–1 fn can also be observed for axial force, radial force, and τ_b for six blades due to the influence of vortices in the vaneless space. The low-frequency pulsations of pressure, force and τ_b are much greater under the low head and high head condition than that under rated head condition. The amplitude of pulsation of various parameters is the smallest under the low flow and rated head compared to that under the low flow conditions of other heads. The flow passage under low head is more influenced by the flow rate. Low-frequency pulsations occur under both the low flow and medium flow conditions. The asymmetry of the flow in the vaneless space causes unbalanced force and hydraulic instability of the runner, which seriously threatens the safe and stable operation of the turbine.

Keywords: Kaplan turbine; CFD; pressure pulsation; hydraulic force; off-design conditions

check for updates

Citation: Liu, C.; Chen, T.; Kang, W.; Kang, J.; Zhou, L.; Tao, R.; Wang, Z. Study on Pressure Pulsation and Force Characteristics of Kaplan Turbine. *Water* **2023**, *15*, 2421. https://doi.org/10.3390/w15132421

Academic Editor: Giuseppe Pezzinga

Received: 24 May 2023
Revised: 21 June 2023
Accepted: 22 June 2023
Published: 30 June 2023

Copyright: © 2023 by the authors. Licensee MDPI, Basel, Switzerland. This article is an open access article distributed under the terms and conditions of the Creative Commons Attribution (CC BY) license (https://creativecommons.org/licenses/by/4.0/).

1. Introduction

China's total energy consumption is large and ranks first in the world with carbon dioxide emissions of about ten billion tons. In order to alleviate this phenomenon, it is necessary to prioritize conservation and deeply implement the concept of development and conservation. Water resources are the world's most important renewable energy source, providing one-fifth of the world's electricity supply. Hydropower can respond quickly to changing electricity demand and improve the continuity of energy supply and the stability of the power grid [1]. The development of Kaplan turbine can reduce migration, protect the environment and maintain ecological balance. Kaplan turbine is very suitable for the green requirements of overfishing. Therefore, Kaplan turbine is one of the key development models for medium and low head power stations in the future [2,3]. The

guide vanes and blades of the Kaplan turbine can be connected to make adjustments to the turbine's operating condition. It is an excellent model worthy of wide use because it can significantly improve the quality of turbine output under variable head, increase the average efficiency of the turbine, and expand the range of stable operation [4]. However, the stability is an important factor to limit the operation of Kaplan turbine in the process of practical application. Because the stability determines whether the turbine unit can operate safely and normally. The factors affecting stability are mainly in three categories: hydraulic factors, structural factors and operating conditions of power station. Hydraulic factors mainly include pressure pulsation, torque, axial force, radial force, and the cam-coordinate relation between guide vanes and blades. Pressure pulsation is one of the main indicators to characterize the stability of turbines [5–7], which is mainly caused by runner–stator interaction and vortex rope in draft tube [8–10]. The resonance phenomenon occurs when the pressure pulsation frequency is the same as the natural frequency of the turbine, which can cause damage to the structure and threaten the safety of the power plant [11–15]. Therefore, a large number of scholars have conducted experiments and simulations on pressure pulsation [16–20]. Both Li et al. [21] and Gao [22] investigated the pressure pulsation of a low specific speed Kaplan turbine by collecting test data on pressure pulsation in the spiral case, the vaneless space and the draft tube through model tests. They came to a similar conclusion that the pressure pulsation induced by the vortex rope of the draft tube is transmitted upstream at low frequencies to the vaneless space as well as to the inlet of the spiral case. The pressure pulsation in the vaneless space is generated by the runner–stator interaction of the blades and guide vanes. The frequency components such as rotational frequency appear in the full flow passage due to the effect of runner–stator interaction. The value of pressure pulsation varies with the power at each location. The higher the power of turbine, the lower the pressure pulsation value in the inlet of the spiral case and the vaneless space, and the higher the pressure pulsation value in the draft tube. Zhu [23] et al. measured the pressure pulsation in an Kaplan turbine with variable cavitation factor, and the results of the data analysis showed that the amplitude of pressure pulsation in the draft tube increases with the development of cavitation. Cavitation in the rim and hub of the Kaplan turbine also affects the pressure pulsation [24,25]. With the continuous development of computer technology, more and more simulation techniques have been applied to turbine calculations [6,16,26–28], which is of great significance to the development of water resources and hydropower [29,30]. Lui et al. [7] predicted the pressure pulsation of an Kaplan turbine by full flow passage unsteady numerical simulation. The prediction results were verified by model tests, and it was concluded that the main pressure pulsation in the draft tube is the low-frequency pressure pulsation caused by vortex rope. The effect of cavitation on pressure pulsation in axial flow turbines has also been studied [11,12,31]. It is found that under off-design conditions, especially under low flow conditions, the flow will separate and generate vortices after the guide vane due to the difference between the actual value of the unit flow and the design value of the flow. This inevitably has some effect on the runner radial force [32]. The vortices consume energy and cause a change in the axial force when the pressure at the inlet of the draft tube is continuously reduced. Zhou et al. [33] studied the operating characteristics of a prototype Francis turbine under off-design conditions, especially the pressure pulsation and axial thrust pulsation under partial load conditions. The pressure pulsations in the vaneless space, runner and draft tube were analyzed in detail. The rotational frequency of the vortex rope in draft tube is 0.24 times the rotational frequency and is transmitted upward from the draft tube to the vaneless space. Due to the influence of vortices, pressure fluctuations, axial and radial forces in the flow field will fluctuate, and τ_b for six blades will also be uneven. The hydraulic torque of guide vanes and blades are the basis for the design of the water guide mechanism and the catcher, runner and operating mechanism respectively. The hydraulic torque needs to include the maximum hydraulic torque of blades and guide vanes under the maximum head in all opening operating range. A small shift in the blade angle also has a large effect on

the torque. Luo [34] reduced the blade angle by 0.5 degrees in the design condition and conducted unsteady flow field calculations. Through the curve of τ_b, it can be seen that due to the angle change of the blades, the average τ_b of blades 1, 2, and 6 have undergone significant changes. Among them, the average τ_b of blade 6 increases, while the average τ_b of blades 1 and 2 decreases. However, there is no significant change in the amplitude and phase sequence of the pulsation of τ_b for six blades. In summary, the unstable flow of turbines under off-design operating conditions consumes energy, changes the pressure in the flow field, and causes changes in axial force, radial force, and torque. Therefore, studying the forces acting on the runner under different operating conditions is of great significance for the safe operation of turbines. This article focuses on the prototype Kaplan turbine, selecting three types of heads: high head, rated head, and low head. Three different flow rates (high flow, medium flow, and low flow) are selected for each head. A total of nine different operating conditions are used in the Computational Fluid Dynamics(CFD) to simulate and calculate the unsteady values of the full flow passage of the turbine. The pressure pulsation in the vaneless space and runner passage of the turbine under different operating conditions is analyzed, and the characteristics of pressure, axial force, radial force, and τ_b pulsation in different regions of the turbine are explored, as well as their variation with operating conditions. By analyzing the internal flow field in the vaneless space under low flow conditions, the relationship between the internal flow in the vaneless space and pressure, runner force, and τ_b pulsation is explored.

2. Numerical Method

2.1. General Equation

The internal Reynolds number of Kaplan turbine is very high, and the flow is nonlinear, multi-scale and unsteady complex turbulent flow. It is generally difficult to directly solve the NS (direct numerical simulation) equation with a computer. Therefore, current research generally simplifies the turbulence model appropriately, ignoring some unimportant details. The Reynolds averaging method, which is a non-direct numerical simulation method used in this article, decomposes turbulent velocity and pressure into the sum of mean and pulsation. This article mainly focuses on the conversion of mechanical energy, so the internal flow control equations of the turbine only have mass conservation equations and energy conservation equations. For the internal flow of fluid machinery, it can be considered that the fluid is incompressible, and its flow law is described by the following basic fluid dynamics equations:

$$\frac{\partial}{\partial x_i}(\overline{u_i}) = 0 \tag{1}$$

$$\frac{\partial}{\partial t}(\overline{u_i}) + \frac{\partial}{\partial x_j}(\overline{u_i u_j}) = -\frac{1}{\rho}\frac{\partial \overline{p}}{\partial x_i} + \frac{\partial}{\partial x_j}\left[\nu\left(\frac{\partial u_i}{\partial x_j} + \frac{\partial u_j}{\partial x_i}\right)\right] - \frac{\partial \overline{u_i' u_j'}}{\partial x_i} + f_i \tag{2}$$

u_i, u_j are the three directional components of velocity in the Cartesian coordinate system system.x_i, x_j are the coordinates.The indicators i and j represent the three-dimensional coordinate direction.f_i is the volume force. v is the kinematic viscosity. t is the time. p is the pressure.

The RANS equation is similar to the original NS equation, and only a new unknown Reynolds stress is introduced, so the equations are closed by connecting the Reynolds stress with the turbulence mean.

2.2. Turbulence Model

Turbulence models are generally two-equation turbulence models that solve for velocity scales and length scales. Through the continuous development of computational flow dynamics, various turbulence models with different characteristics have emerged. The turbulent kinetic energy k is the average amount of kinetic energy per unit mass of pulsating motion. The vortex viscous model uses the Boussinesq assumption. The Reynolds stress is

analogous to the viscous stress, and the Reynolds stress is considered to be related to the mean velocity gradient and the vortex viscosity coefficient. The relationship is as follows.

$$\overline{-u_i u_j} = v_t \left(\frac{\partial \overline{u_j}}{\partial \overline{x_j}} + \frac{\partial \overline{u_j}}{\partial x_i} \right) - \frac{2}{3} k \delta_j \tag{3}$$

The vortex viscosity coefficient v_t is mainly based on the $k-\mathcal{E}$ model, the $k-\omega$ model and the corresponding improved models, which are mainly based on the equations related to the turbulent energy k and the turbulent dissipation rate $\mathcal{E}$ or turbulent frequency ω to close the equations. The equations for turbulent energy k and dissipation rate $k-\mathcal{E}$ are as follows.

$$k = \frac{1}{2} \overline{u_i' u_j'} \tag{4}$$

$$\varepsilon = \nu \overline{\left(\frac{\partial u_i'}{\partial x_j} \right) \left(\frac{\partial u_i'}{\partial x_j} \right)} \tag{5}$$

The $k-\mathcal{E}$ turbulence model is more accurate when simulating three-dimensional fluid turbulent flow and is a high Reynolds number turbulence model. However, there are deviations in the calculation of anisotropy that requires consideration of turbulent viscosity, and it is difficult to accurately predict wall flow or flow with backflow and strong vortices. RNG$k-\mathcal{E}$ modified the transport equation for the dissipation rate $\mathcal{E}$, taking into account factors regarding the rotation rate and strain rate, which improved for the simulation of rotational turbulence and large curvature flow [35,36].Unlike the $k-\mathcal{E}$ model, which is insensitive to the inverse pressure gradient and always models excessive shear stresses, the $k-\omega$ model improves the accuracy of boundary layer calculations by introducing turbulent kinetic energy k and turbulent frequency ω to make the time-averaged N-S equation closed and does not contain the nonlinear damping function necessary in the $k-\mathcal{E}$ model.The $k-\omega$ model does not differ much from the actual results in the calculations of outflow wake, mixed flow and cylindrical bypass flow, but in free shear flow, the turbulent dissipation rate ω has a disproportionate effect on the $k-\omega$ model results. The vortex viscosity coefficient in the standard $k-\omega$ model is defined as:

$$v_t = \frac{k}{\omega} \tag{6}$$

The SST $k-\omega$ (Shear Stress Transport $k-\omega$ Model) combines the $k-\mathcal{E}$ model and the $k-\omega$ model. $k-\omega$ model in the near-wall region and the $k-\mathcal{E}$ model in the turbulent core [37,38]. The SST model predicts flow separation well due to its coupling nature, which takes into account the transport of turbulent shear stresses. The SST $k-\omega$ model has a greater advantage in predicting near-wall flow and flow with an inverse pressure gradient.

$$\frac{\partial(\rho_{\mathrm{m}} k)}{\partial t} + \frac{\partial(\rho_m u_i k)}{\partial t} = P_k - \frac{\rho_m k^{3/2}}{l_{k-\alpha}} + \frac{\partial}{\partial x_i} \left[\left(\mu + \frac{\mu_c}{\sigma_k} \right) \frac{\partial k}{\partial x_i} \right] \tag{7}$$

$$\frac{\partial(\rho\omega)}{\partial t} + \frac{\partial(\rho u_i \omega)}{\partial x_i} = C_\omega P - \beta \rho \omega^2 + \frac{\partial}{\partial x_i} \left[(\mu_l + \sigma_\omega \mu_t) \frac{\partial \omega}{\partial x_i} \right] + 2(1 - F_1) \frac{\rho \sigma_{\omega 2}}{\omega} \frac{\partial k}{\partial x_i} \frac{\partial \omega}{\partial x_i} \tag{8}$$

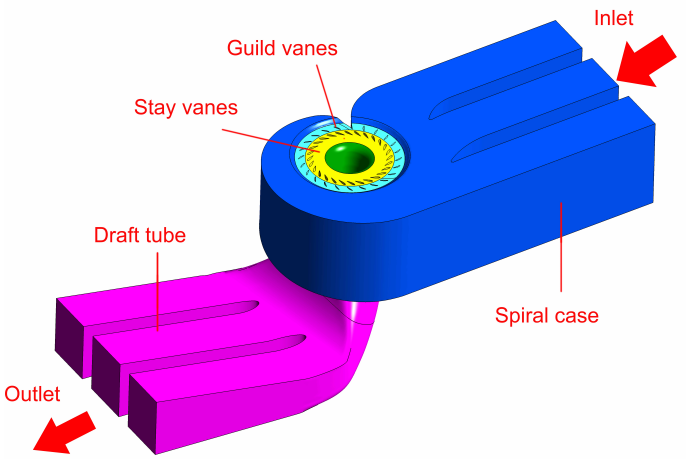
ρ_m is fluid density, P is the turbulence generation term, F_1 is the mixing function, k is the turbulent kinetic energy, ω is the turbulence frequency, $\boldsymbol{\mu}$ is the kinetic viscosity, and the empirical coefficients $\sigma_k = 2$, $\beta = 0.0828$, $\sigma_{\omega 2} = 0.856$.

3. Numerical Settings

3.1. Computational Domain and Parameters of Kaplan Turbine

The three-dimensional modeling of a full-flow passage of an Kaplan turbine is shown in Figure 1 below. Considering the shape and structure of each flow passage of the turbine, the fluid domain is divided into five parts for 3D modeling, including the spiral case, stay

vane, guide vane, runner, and draft tube. The main performance parameters of Kaplan turbine are shown in Table 1 below.



(**a**) Model



(**b**) Prototype

Figure 1. Three-dimensional modeling and prototype of the full-flow passage of the Kaplan turbine.

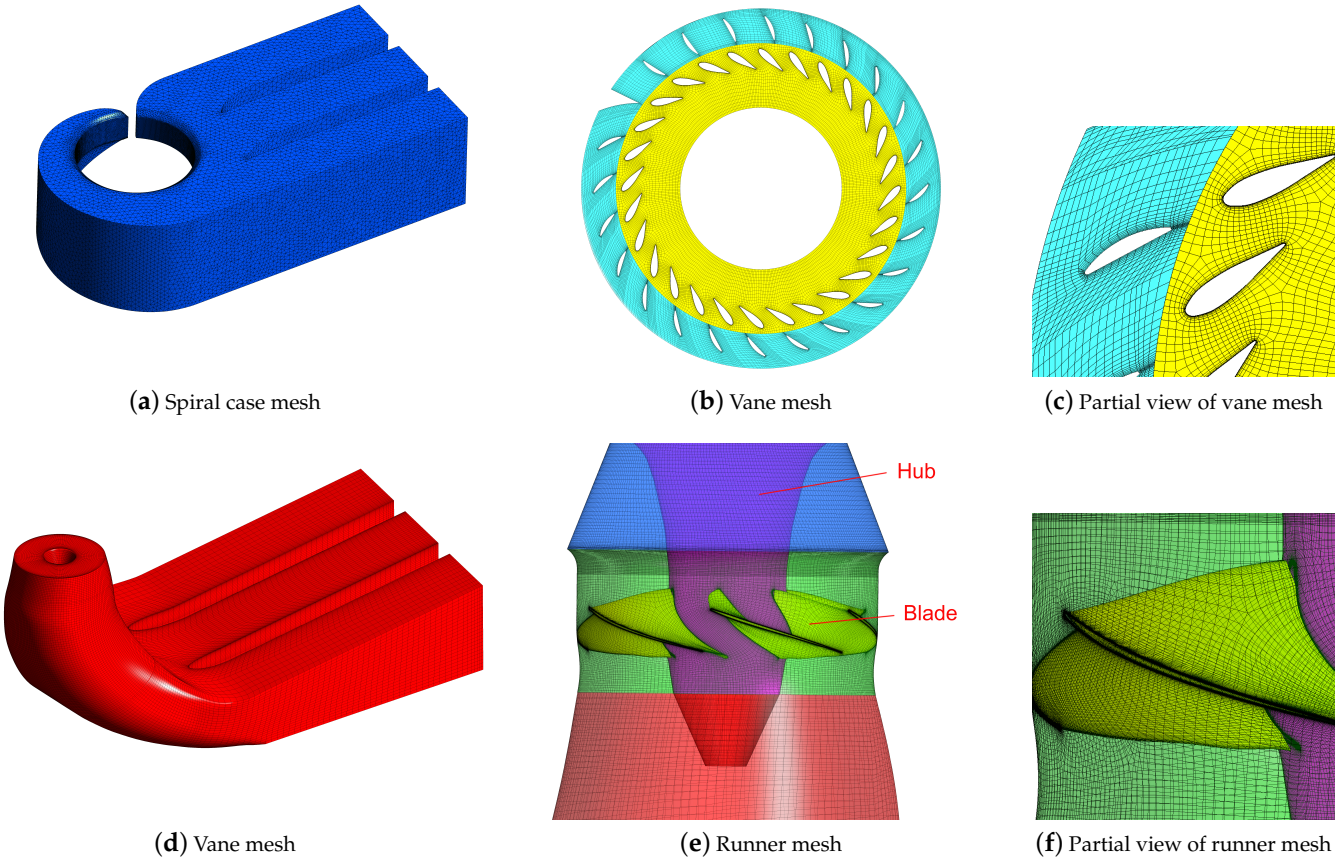
Table 1. Parameters of Kaplan turbine.

Prototype Turbine	Value
Rotating speed of the rotor n	68.2 r/min
Number of stay vanes Zs	25
Number of guide vanes Zg	28
Number of blades Zr	6
Diameter of the rotor D	10.4 m
Rated head Hr	25 m

3.2. Meshes and Calculation Conditions Setting

In this paper, structured hexahedral mesh and unstructured tetrahedral mesh are selected to divide each fluid domain of the turbine separately. The number and size of meshes of critical passages are controlled to improve computational accuracy and efficiency. The runner and guide vane passage are divided into structured meshes by TurboGrid. The meshes of the runner passage is increased to ensure the accuracy of force and torque calculations. ICEM is used to divide the fluid domain of stay vanes and draft tube into structured meshes, and the meshes are properly adjusted and smoothed. The spiral case

fluid domain is divided by unstructured tetrahedral mesh due to its complex structure. The meshes of each flow passage are shown in Figure 2.



(**a**) Spiral case mesh (**b**) Vane mesh (**c**) Partial view of vane mesh

(**d**) Vane mesh (**e**) Runner mesh (**f**) Partial view of runner mesh

Figure 2. Mesh of flow passages.

3.3. Mesh Independence Check

An increase in the number of meshes can make the simulation results more consistent with the experimental results, but an excessive number of meshes can lead to a larger computational cost. Therefore, in order to ensure the accuracy of the numerical simulation, it is necessary to check the mesh independence to select the most suitable set of meshes. In this paper, the mesh independence is analyzed based on the variation of the efficiency of the prototype Kaplan turbine under rated operating conditions.The result is shown in Figure 3. The blade angle is 0° and the guide vane opening is 30° under rated operating conditions. The boundary conditions and the opening of blades and guide vanes are kept constant, and four sets of meshes are created for the calculation. The measured results of the prototype turbine and the calculated results of each set are shown in Table 2.

Table 2. Different sets of meshes (elements:10^4).

	Spiral Case	Stay Vane	Guild Vane	Runner	Draft Tube	Total	Efficiency
set1	31	23	63	185	27	329	91.03%
set2	60	30	61	235	58	444	92.03%
set3	77	35	90	248	83	533	92.81%
set4	101	45	132	295	104	677	92.86%
Field measurement							93.02%

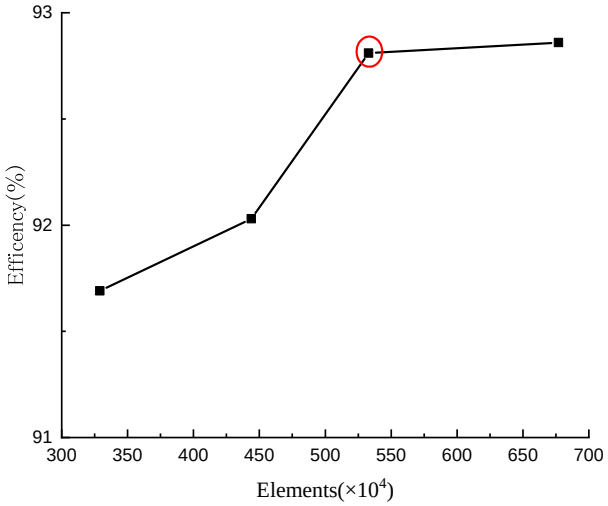


Figure 3. Mesh independence analysis.

3.4. Boundary Conditions and Monitoring Point Settings

The calculation in this article is carried out using ANSYS CFX software. The calculation model is SST $k-\omega$ model. The volute inlet is set as the total pressure inlet, and the draft tube outlet is set as the static pressure outlet. The runner passage is set as a rotating passage, while the other passages are set as stationary passage. During steady calculation, the connection method between the runner and stator interfaces is set to Stage Rotor, while the other interfaces are set to General Connection. The convergence residual of steady calculation is set to 10^5. In unsteady calculations, the connection method between the runner and stator interfaces is set to Transient Rotor Stator. Then the steady calculation results are used as the initial conditions for unsteady calculations. The unsteady calculation time step is taken as 1/252 of the time one revolution of the runner, and 20 cycles are calculated. In order to study the pressure pulsation at different positions inside the turbine, some pressure pulsation monitoring points are arranged in each passage of the Kaplan turbine. Seven monitoring points VL1 to VL7 are arranged along the flow direction in the vaneless space. Two measuring points, RU1 and RU2, are uniformly distributed at the entrance of the runner passage. All monitoring points are fixed and do not rotate with the runner. The location of monitoring points is shown in Figure 4.

3.5. Determination of Monitoring Points

The Kaplan turbine has a wide operating range and exhibits different pressure pulsation characteristics in different operating conditions, which affects the stability and reliability of the turbine. Within the normal operating area of the turbine, three kinds of heads (maximum head, rated head, and minimum head) of the prototype Kaplan turbine are selected. The operating conditions of each head are divided into three kinds of flow rate (high flow, medium flow, and low flow). A total of nine operating points are used for unsteady numerical simulation. The parameters for each condition are shown in Table 3.

In order to facilitate the analysis, the pressure of each monitoring point in the turbine is represented by the pressure coefficient C_p. The speed is represented by the speed coefficient C_v. The dimensionless number $\triangle H/H$ obtained by dividing the amplitude of pressure pulsation by the rated head is used to represent the pressure amplitude.

$$C_p = \frac{P}{1/2\rho v_0^2} \tag{9}$$

$$C_V = \frac{v}{\frac{\pi n D}{60}} \tag{10}$$

$$\frac{\Delta H}{H} = \frac{\frac{A_P}{\rho g}}{H} \times 100\% \tag{11}$$

P-pressure pulsation value at the measurement point, Pa. ρ-the density of water, kg/m^3. v_0 -inlet velocity of the spiral case under rated condition, 1.76 m/s. v-velocity of the monitoring point, m/s. A_P-the amplitude of the pressure pulsation at the measurement point, Pa. H is the rated head H_r.

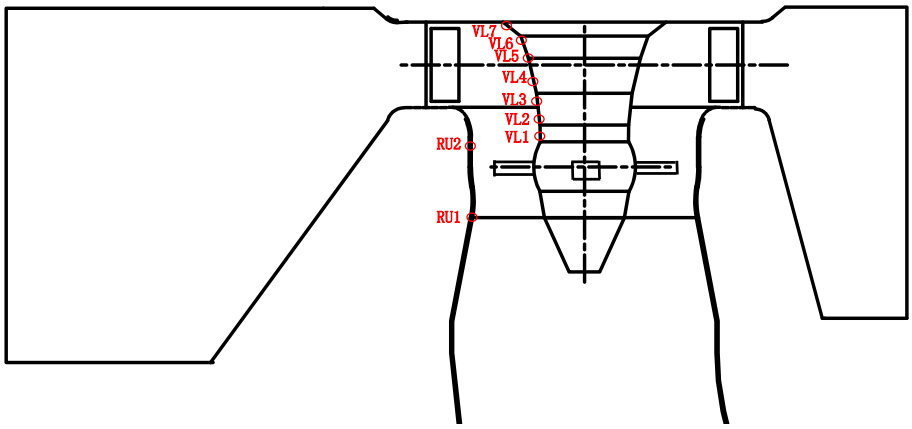


Figure 4. Location of monitoring points.

Table 3. Different conditions.

Head	Condition	Blade Angle (°)	Angle of Guide Vane (°)	Flow Rate (m^3/s)
37.79 m (maximum head)	1	−15.693	17.83	290.8 (Low flow)
	2	−4.959	25.152	565.2 (Medium flow)
	3	−0.995	27.428	669.2 (high flow)
25 m (rated head)	4	−14.289	21.843	301.8 (Low flow)
	5	−4.959	31.388	554.5 (Medium flow)
	6	7.344	44.306	930.6 (high flow)
12.91 m (minimum head)	7	−13.381	34.949	325.9 (Low flow)
	8	−4.959	46.193	552.2 (Medium flow)
	9	4.454	56.826	828.3 (high flow)

4. Results

4.1. Pressure Pulsation

The pressure pulsation characteristics are studied by setting monitoring points in the vaneless space and runner passage, and the location of the monitoring points are shown in Figure 4. The monitoring points VL1-7 are the seven monitoring points arranged along the flow direction in the vaneless space. Figure 5 shows the frequency–domain of each monitoring point. The frequency–domain patterns of monitoring points VL1 VL 7 of condition 1 are the same and the 1 fn with larger amplitude is observed. The main frequency of the pressure monitoring points of conditions 2 and 3 is 6 fn, which is the blade passing frequency, and there is no high amplitude of low frequency. The monitoring results of the remaining heads have similar patterns. There are low frequency pulsations at low flow in both condition 4 and condition 7, with frequencies of 0.9 fn and 0.5 fn, but the amplitude is relatively small. As the flow rate increases at the rated head, the main frequency of the monitoring point is 6 fn, and the low-frequency disappears. Under low head, as the flow rate increases, low-frequency still exists, but its amplitude is much smaller than that of 6 fn. The maximum amplitude is at VL1, which is closest to the runner, among the seven monitoring points under all operating conditions. The smallest amplitude is at VL7 in the vaneless space. When the head is certain, the amplitude of 6 fn in the vaneless space gradually increases with the increase of flow.

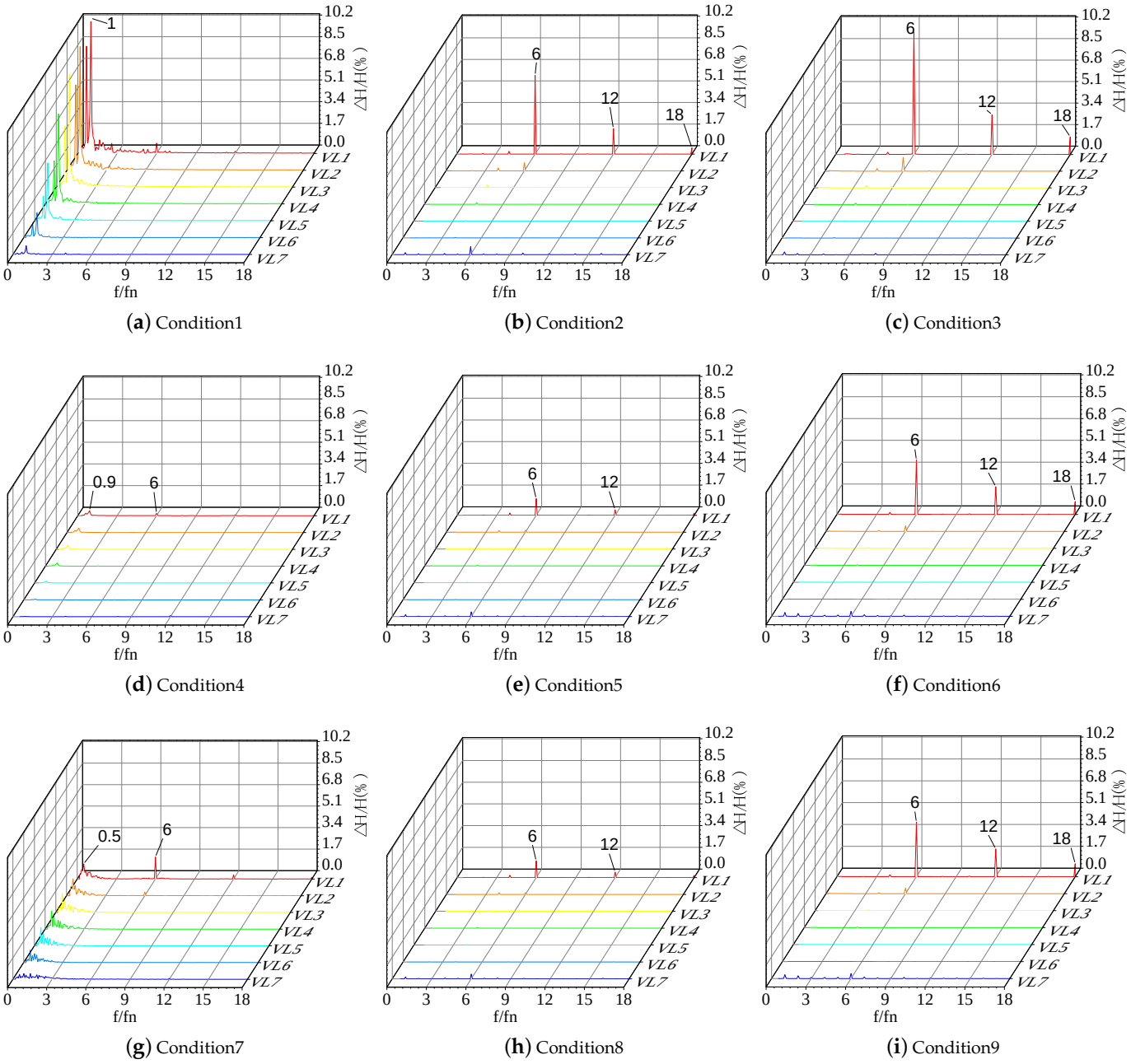


Figure 5. Frequency-domain of pressure pulsation at monitoring points in the vaneless space.

Monitoring points YL3 and YL5 are arranged on the wall to monitor the inlet and outlet pressure pulsations of runner passage. YL3 is above the runner and YL5 is under the runner. The frequency–domain of the monitoring points in the runner passage are shown in Figure 6. The low-frequency characteristics and amplitude of the runner inlet are obvious except for 6 fn in the low flow condition 1. The amplitude of 1 fn is the largest, and the amplitude is 2.4 times of that of 6 fn. However, 6 fn is still the main frequency of the runner outlet, and the amplitude of 1 fn is very small. The main frequencies of the remaining low flow conditions 4 and 7 are 6 fn and its harmonic frequencies, with small amplitude of low-frequency components. When the head is certain, the amplitude of 6 fn in the runner increases gradually with the increase of the flow rate, which is similar to the law in the vaneless space.

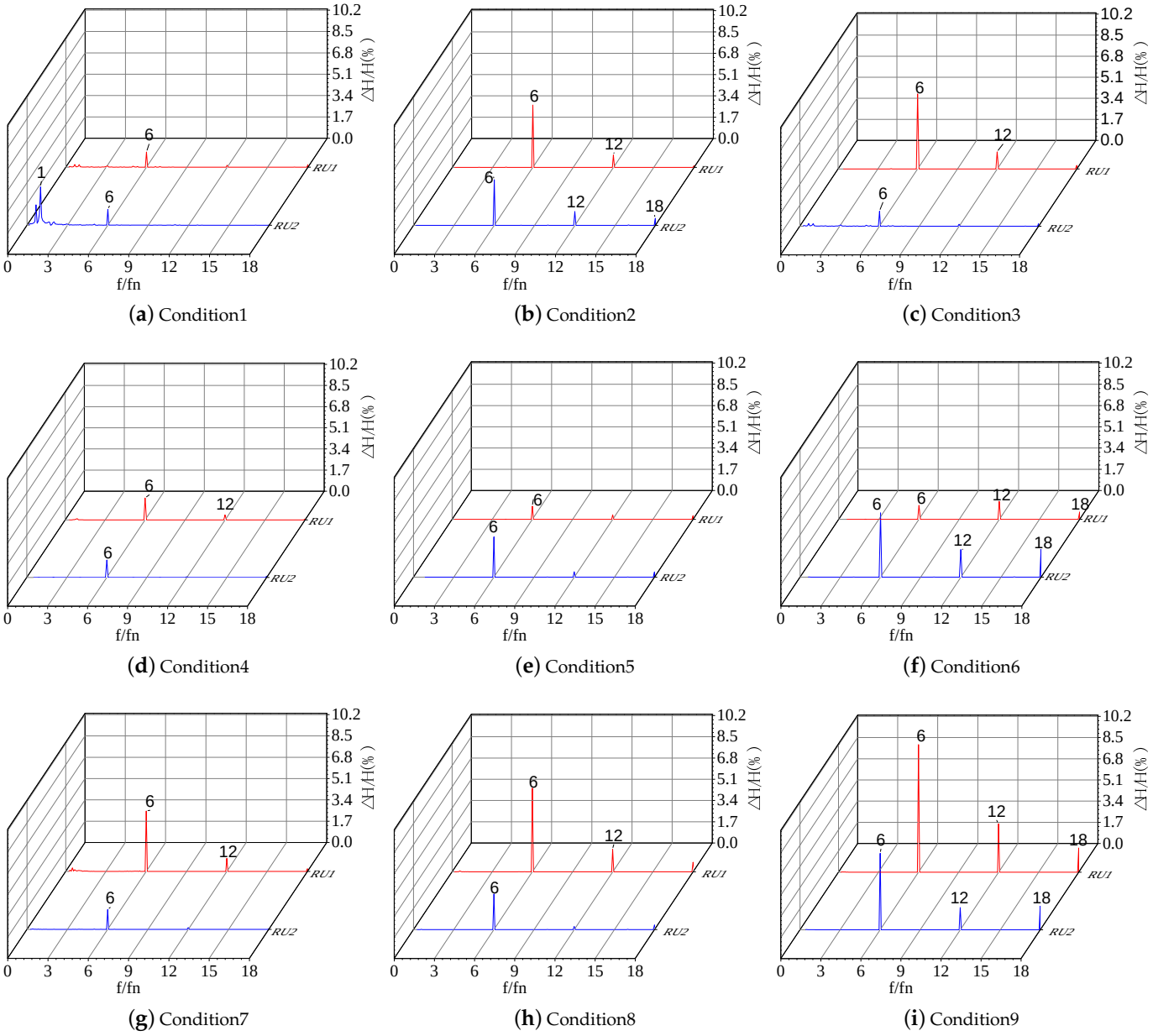
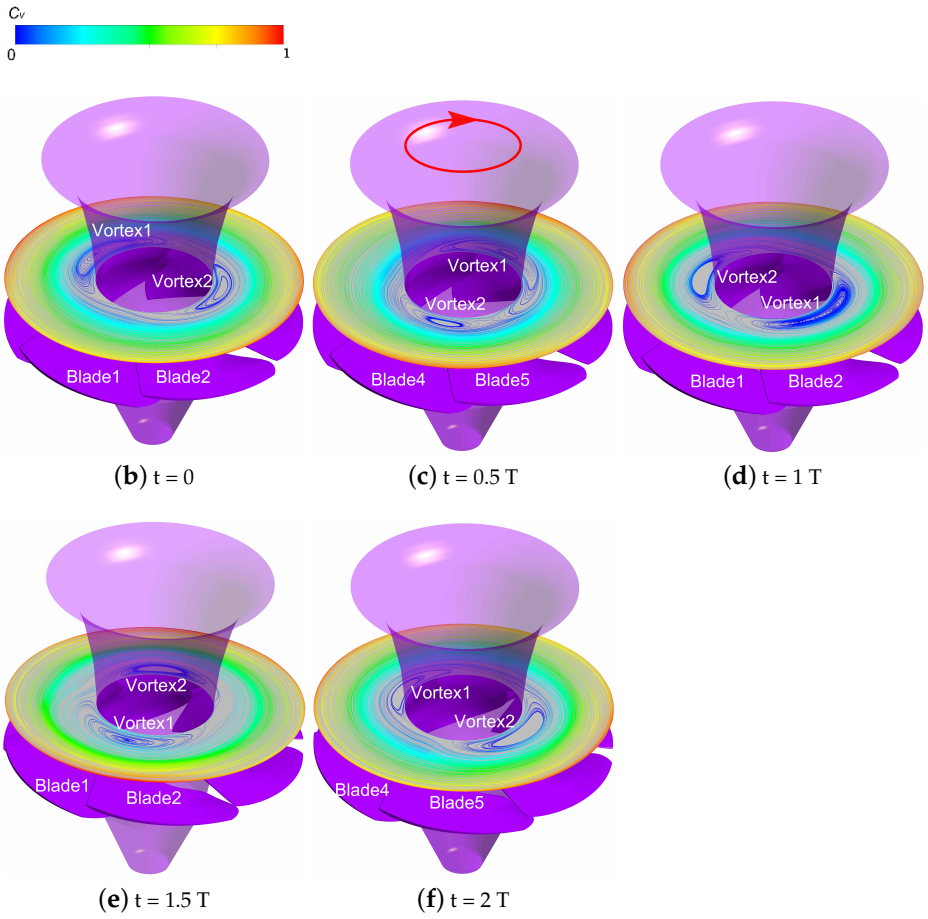


Figure 6. Frequency-domain of pressure pulsation at monitoring points in the runner passage.

4.2. Vortices in the Vaneless Space

The structure of the Kaplan turbine determines that it has a large space in the vaneless space between the outlet of the guide vane and the inlet of the runner blades. In the study of the pressure pulsation characteristics for different conditions in various passages of the turbine, it is found that there are relatively obvious low frequencies of pressure pulsation in the vaneless space under low flow and different heads, such as 1 fn in condition 1, 0.9 fn in condition 4, and 0.5 fn in condition 7. Therefore, the flow field in the vaneless space is analyzed. Figure 7 shows the blade position and streamline distribution on the horizontal cross-section of the turbine for condition 1 at four moments: t = 0.3 T, t = 0.6 T, t = 1 T and t = 2 T. It can be seen that the flow from the outlet of the guide vane forms two vortices with a phase angle difference of nearly 180 degrees before entering the runner. In the stationary coordinate system, vortices rotate in the same direction as the runner. The rotating frequency of vortices is about half of the rotational frequency, which is 0.5 fn. Since there are two vortex zones, the pressure pulsation frequency at the monitoring point in the

stationary coordinate system is about 1 fn. Therefore, the 1 fn monitored in the pressure pulsation in the condition 1 is mainly affected by the vortices in the vaneless space. Figure 8 shows the blade position and streamline distribution on the horizontal cross-sections of condition 4 at t = 0, t = 0.5 T, t = 1.1 T three moments. It can be seen that there are also two vortices in the vaneless space, and the position of vortex 3 is basically unchanged. With the rotation of the runner, vortex 4 will fall off from vortex 3, rotate along clockwise, and then go around in a circle before returning to vortex 3. The entire cycle is roughly 1.1 T, so a frequency of 0.9 fn is detected in the pressure pulsation in the vaneless space of case 4. Figure 9 shows the blade positions and the streamline distribution on the vertical cross-sections for condition 7 at three moments: t = 0, t = 1 T, and t = 2 T. The vortices appear on the upper side of the vaneless space, and there are differences in the vortex patterns of each cross-section. These vortices at different positions in the circumferential direction move periodically up and down near the hub surface as the runner rotates. The size of vortices also changes, reaching a maximum near the guide vane and a minimum near the blade. The period of the whole process is 0.5 fn.



(**b**) t = 0 (**c**) t = 0.5 T (**d**) t = 1 T

(**e**) t = 1.5 T (**f**) t = 2 T

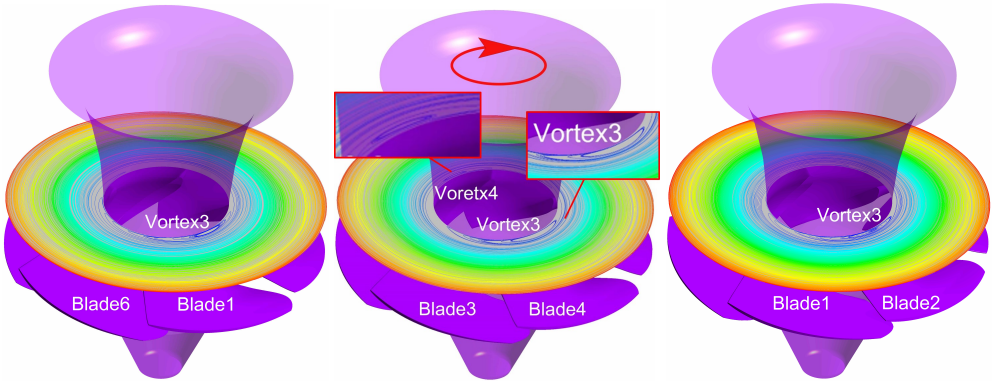
Figure 7. Vortices in the runner passage at different moments of condition 1.

4.3. Radial Force

In this paper, the value of the combined force F on the runner is solved by the force components F_x and F_y received by the surface of the runner (including hub and blade) in the x and y directions. The value of F and directional angle of the combined force θ_F are:

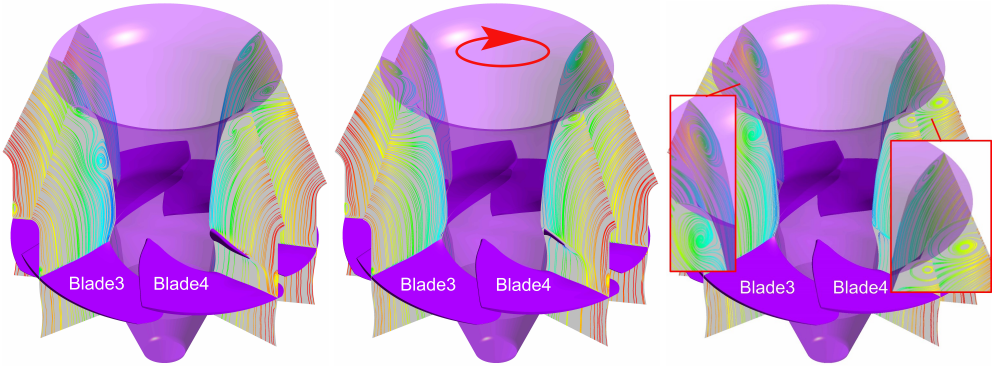
$$F = \sqrt{{F_x}^2 + {F_y}^2} \tag{12}$$

$$\theta_F = \text{atan}\left(F_y / F_x\right) \tag{13}$$



(**a**) t = 0 (**b**) t = 0.5 T (**c**) t=1.1T

Figure 8. Vortices in the runner passage at different moments of condition 4.

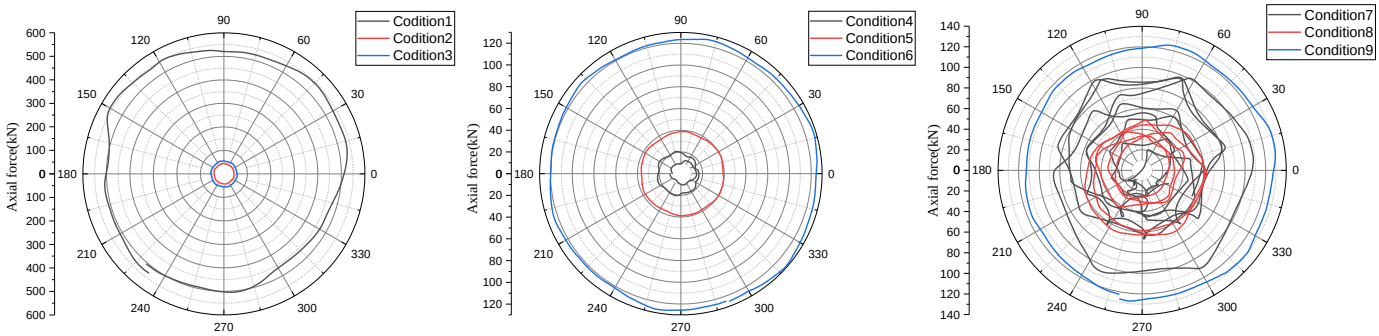


(**a**) t = 0 (**b**) t = 0.5 T (**c**) t = 1 T

Figure 9. Vortices in the runner passage at different moments of condition 7.

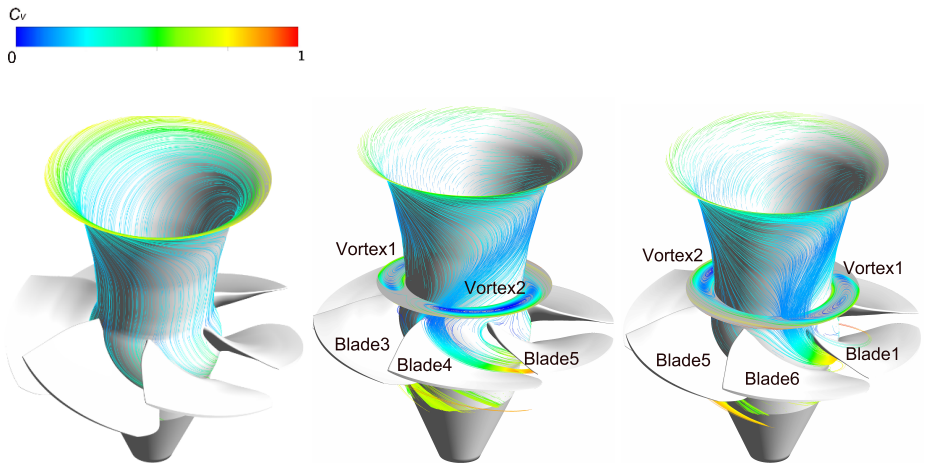
Figure 10 shows the polar of the radial force of different conditions under three heads, indicating the value and direction of the radial force for each operating condition within a change cycle. The radial force change period of condition 1 is 3 T, the radial force change period of condition 4 is 1.9 T, the radial force change period of condition 7 is 12 T, the radial force change period of condition 8 is 5 T, and the radial force change period of the remaining conditions are 1 T. Figure 10 shows that the radial force in low flow condition 1 is between 460 kN and 550 kN, which is much larger than that of other conditions under high head. The radial force of condition 6 is about 120 kN, which is 80 kN larger than that of other conditions under rated head. The maximum radial force for condition 9 at low head is 115 kN, and the radial force for conditions 7 and 8 fluctuates widely between 20–80 kN. This indicates that as the head increases, the radial force of the runner is greatly affected by the flow rate, and does not always increase with the increase of flow rate. The radial force of the high-flow conditions is obviously smoother in polar coordinates, while the low flow rate tends to cause the fluctuation of radial force. The reason for this phenomenon is related to the streamline distribution law of the vaneless space. Figure 11 shows the streamline distribution in the vaneless space of condition 1 and condition 2. Figure 12 shows the pressure distribution on the horizontal section of the vaneless space at different moments for condition 1. It can be seen that the flow is relatively smooth at the design condition, and the streamlines are evenly distributed among the blades. However, under low flow conditions, vortices in the vaneless space block the passage and force the remaining flow to change its rotation direction, forming two low pressure zones near vortices in the vaneless space. The position of low pressure zone 1 and vortex 1 overlap, and the position of low pressure zone 2 and vortex 2 overlap. The two low pressure zones lead to uneven pressure

distribution on the surface of the runner, resulting in a significant radial force. According to Figure 12, it can be seen that in addition to periodic rotation, the pressure value in the low pressure region within the vaneless space also undergoes periodic changes. The pressure in one low pressure zone has a period of 6 T, therefore the frequency is 0.166 fn, and the frequency of two low pressure zones is 0.33 fn. Figure 13 shows the frequency–domain of the radial force pulsation for different conditions under three heads, and the results show that the main frequencies of the radial force fluctuation for condition 1 are 0.333 fn and 1 fn. 1 fn is caused by rotation of two vortices. 0.33 fn is caused by the periodic change of pressure in two low pressure zones. Influenced by vortices in the vaneless space, the radial force in condition 4 and condition 7 also shows a large value of low-frequency pulsation. Therefore, the flow asymmetry caused by the vortices in the vaneless space under low flow conditions is the main reason for the large radial force of the runner.



(**a**) High head (**b**) Rated head (**c**) Low head

Figure 10. Polar of radial force of runner under different heads.



(**b**) Condition2 (**c**) Condition1 (**d**) Condition1

Figure 11. Streamlines on the hub surface of the runner.

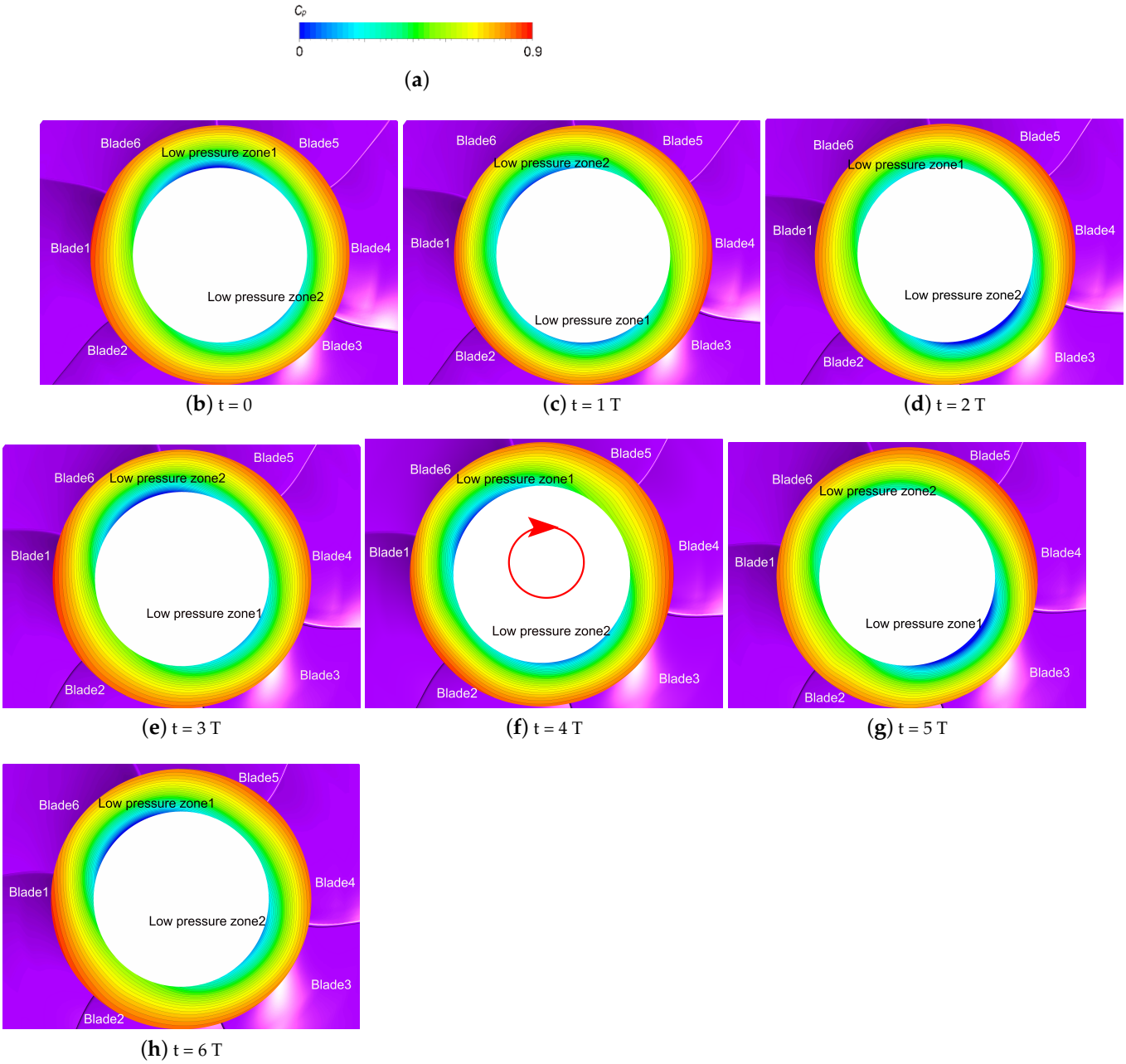


Figure 12. Pressure distribution of horizontal section in the runner passage at different moments of condition 1.

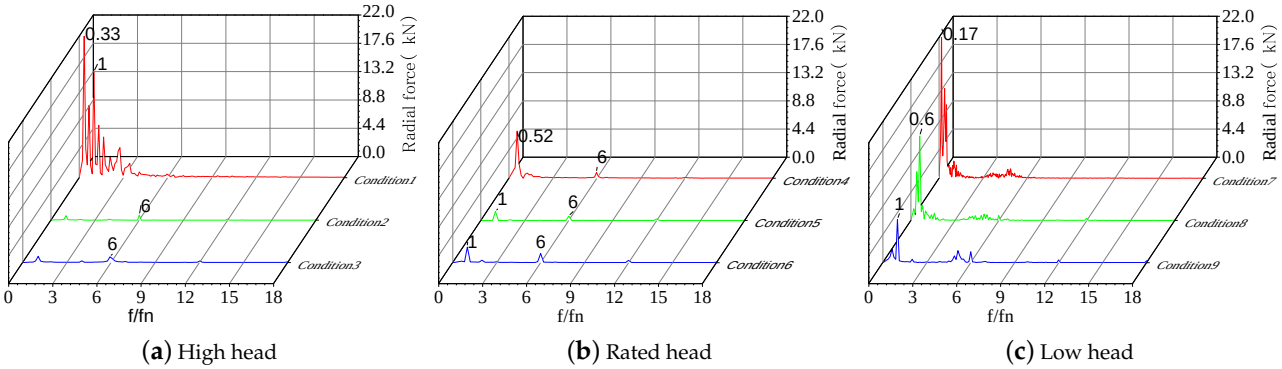


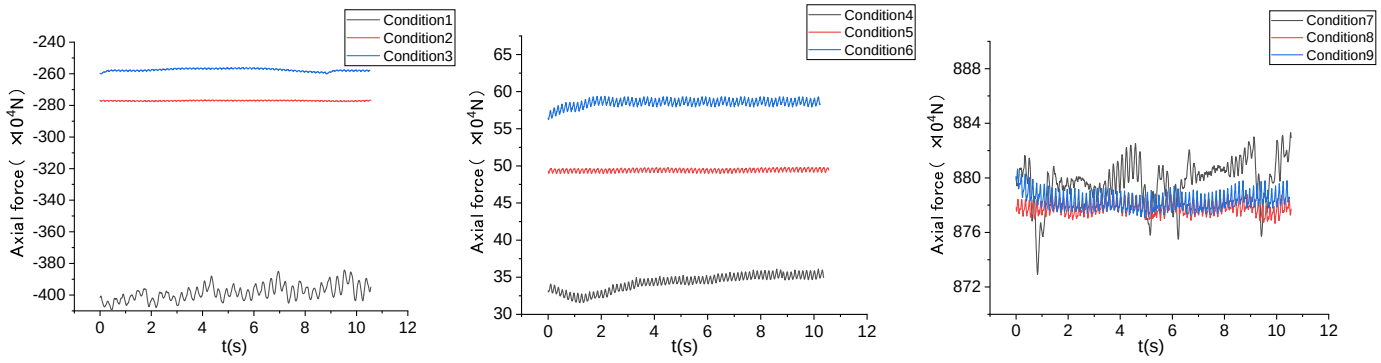
Figure 13. Frequency–domain of radial force pulsation under different heads.

4.4. Axial Force

Figure 14 show the time-domain of axial force of nine operating conditions under three different heads. The axial force of the runner mainly includes the axial force on the hub and blades. The results show that the axial force of three conditions under low head is downward, while the axial force under rated head and high head conditions is upward. The axial force under three low flow conditions fluctuates significantly with the rotation of the runner. The average axial force of the runner in condition 1 is about 400×10^4 N, and the axial force fluctuation is about 10×10^4 N. When the head decreases to the rated head, the axial force of the runner changes from downward along the main shaft to upward. The average axial force of each blade in condition 4 is approximately 32.5×10^4 N, and the axial force fluctuation is about 1×10^4 N.Under low head, the axial force of the runner increases significantly. The average axial force of each blade in condition 7 is about 878×10^4 N, and the axial force fluctuation is about 4×10^4 N. Under low head and rated head, as the flow rate increases, the axial force of the runner upwards continuously increases. Under high head, the axial force of the runner is less affected by the flow rate, but the fluctuation of axial force is the highest under low flow conditions at each head. Figure 15 show the frequency–domain of axial force fluctuations under low flow conditions. The results show that there are large low-frequency fluctuations in axial force under conditions 1 and 7, while the low-frequency amplitude under condition 4 is relatively small. The main frequencies of axial force in condition 1 are 0.33 fn, 1 fn, and 3 fn, the main frequency of axial force in condition 7 is 0.4 fn, and the main frequency of axial force in condition 4 is 6 fn. 0.33 fn of condition 1 is affected by pressure changes in the low pressure zone, 1 fn is caused by the rotation of two vortices in the vaneless space, and 3 fn is related to runner–stator interaction. The rotation frequency of a single vortex in the vaneless space is 0.5 fn, and the blade passing frequency is 6 fn. The node diameter of the interference mode between the two satisfies $nZ_v + k = mZ_r$. The pulsation frequency caused by interference is:

$$f_{vk} = mZ_r f_n - nZ_v f_v \tag{14}$$

For the two vortex regions and six runner blades shown in Figure 7, when $m = 1$, $n = 2$, $k = 2$, $f_{vk} = 3f_n$, it indicates that the axial force is mainly affected by runner–stator interaction. The 0 node diameter mode is the main excitation mode. The 0 node diameter mode is a synchronous mode. Due to the influence of vortices on the runner passage, the force on the runner will fluctuate periodically.



(**a**) High head (**b**) Rated head (**c**) Low head

Figure 14. Time-domain of axial force pulsation under different heads.

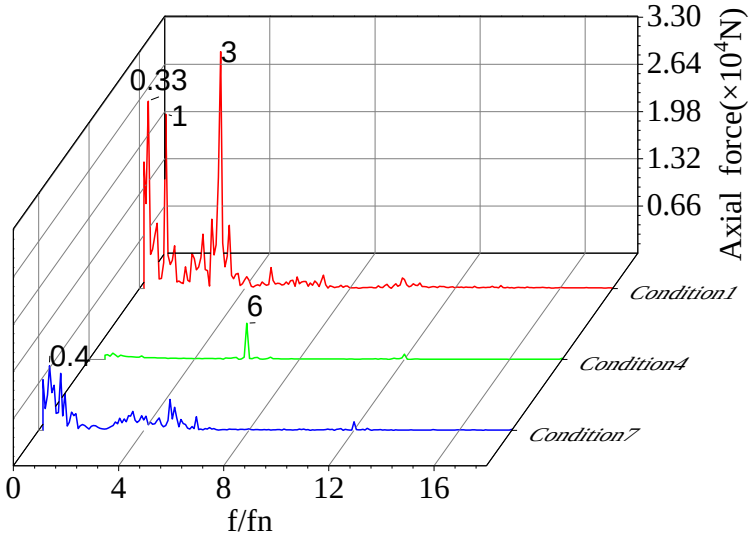


Figure 15. Frequency–domain of axial force pulsation under low flow conditions.

4.5. Hydraulic Torques along Blade Shank(τ_b)

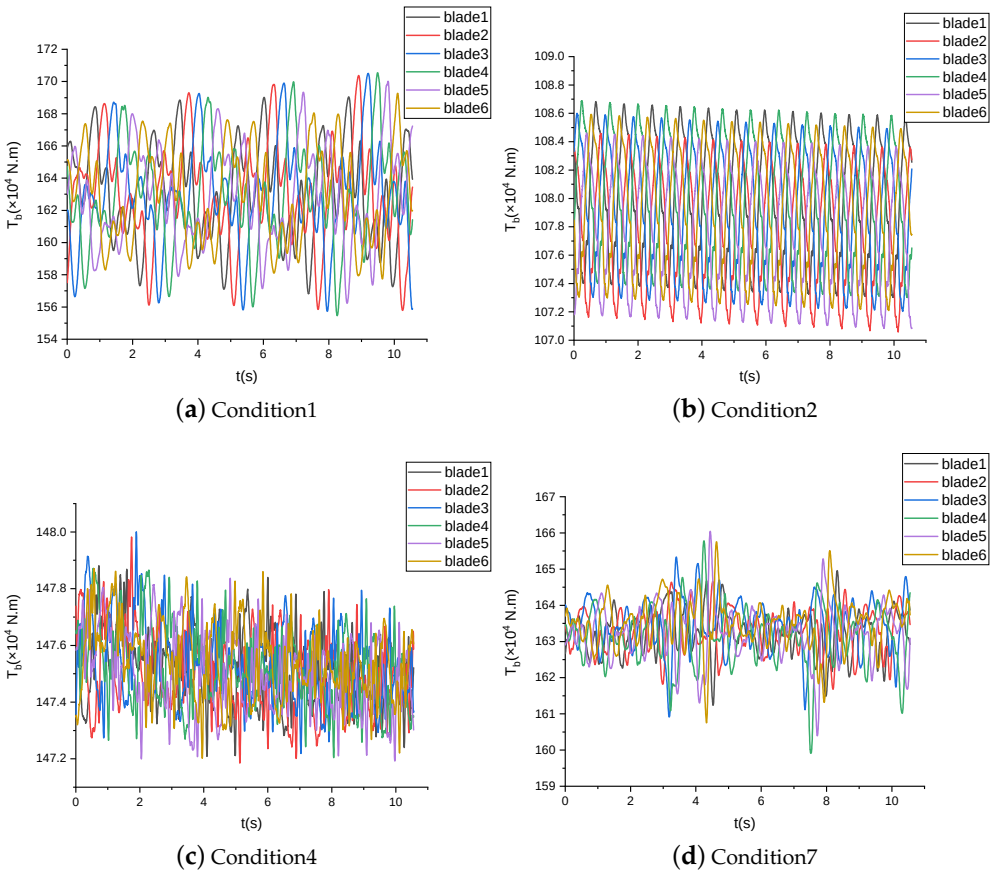
Figures 16 and 17 show the variation of hydraulic torques along blade shank (τ_b) for six blades over time and the frequency domain of torque pulsation. It can be seen that the τ_b of a single blade is unsteady, non-uniform, and asynchronous. Its pulsation amplitude increases with the increase of flow rate under rated head and low head, and the main frequency is the rotational frequency. However, under high head, the main frequency of condition 1 is 0.333 fn, which is consistent with the main frequency of radial force. The amplitude of 0.33 fn is the highest. The main frequency of conditions 2 and 3 is 1 fn. When the head is constant, the τ_b difference between adjacent blades is large at low flow conditions, which is caused by vortices. From the phase of the τ_b pulsation of the six blades, the phase difference between two adjacent blades in condition 2 is 60°, and is arranged in the phase order of blade6, blade5, blade4, blade3, blade2, and blade1. This phenomenon is mainly caused by the uneven circumferential flow of the spiral case and stay vanes. However, the phase difference between adjacent two blades under condition 1 is 120°, mainly due to the uneven flow caused by two circumferential symmetric low pressure zones on the cross-section in vaneless space. Under low flow conditions of other heads, there may also be situations where the phase difference between adjacent blades is not 60°, which is mainly affected by the distribution of vortices in the vaneless space.

5. Conclusions

1. Under low flow conditions, there will be periodic vortices in the vaneless space. Under high head and low flow conditions, two vortices with phase angles nearly 180 degrees apart will form at the inlet of the runner. In a stationary coordinate system, the vortex zone rotates in the same direction as the runner with a rotating frequency of 0.5 fn. Since there are two vortex zones, the pressure pulsation frequency at the monitoring point is about 1 fn. The vaneless space under low head and low flow condition is characterized by vortices with periodic vertical fluctuations, reaching its maximum near the guide vanes and its minimum near the runner blades. The frequency of vortex fluctuations is 0.5 fn. Therefore, under low flow conditions, there will be low-frequency pressure fluctuations of 0.5–1 fn in the vaneless space affected by vortices.
2. Under high head and low flow conditions, vortices block the passage and force flow to change direction. Therefore, a low pressure zone will be generated at the vortex. As the runner rotates, the pressure value in the low pressure zone also undergoes periodic changes. The frequency of pressure change in one low pressure zone is 0.166 fn, and the frequency of pressure change in two low-pressure zones is 0.33 fn. The main

frequencies of radial force fluctuations under high head and low flow conditions are 0.33 fn and 1 fn. 1 fn is caused by the rotation of two vortices and 0.33 fn is caused by periodic changes in pressure values in the two low pressure zones. Therefore, the flow asymmetry caused by vortices in the vaneless space under low flow conditions is the main reason for the large radial force of the runner.

3. Under low head and rated head, the axial force of the runner upwards continuously increases as the flow rate increases. Under high head, the axial force of the runner is less affected by the flow rate. But under each head, the fluctuation of axial force is the highest under low flow conditions. Under low flow of high head and low head conditions, low-frequency pulsation of axial force is generated due to the influence of vortices.
4. The hydraulic torques along blade shank (τ_b) for six blades are unsteady, non-uniform, and asynchronous. The pulsation amplitude of τ_b increases with the increase of flow rate under rated head and low head, and the main frequency is 1 fn. However, under high head and low flow, the main frequency of τ_b is 0.333 fn, which is consistent with the main frequency of radial force, and the amplitude is the largest. The phase difference between adjacent blades under high flow conditions is 60°. The two circumferential symmetrical low pressure zones under high head and low flow conditions cause uneven flow, resulting in a phase difference of 120° between adjacent blades. This state of the blade operating mechanism causes rapid damage to key components.



(**a**) Condition1 (**b**) Condition2

(**c**) Condition4 (**d**) Condition7

Figure 16. Time–domain of τ_b pulsation of different conditions.

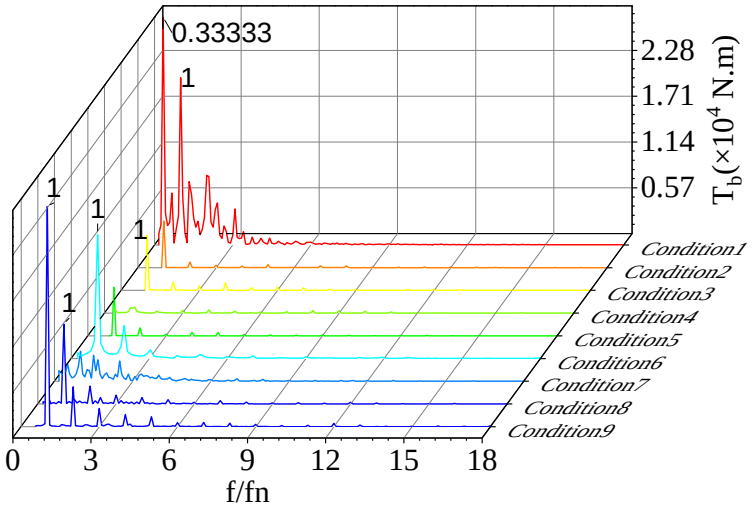


Figure 17. Frequency–domain of τ_b pulsation under low flow conditions.

Author Contributions: Conceptualization, C.L.; methodology, C.L.; investigation, C.L.; validation, T.C. ; writing—original draft preparation, W.K.; writing—review and editing, C.L. and J.K.; supervision, L.Z., R.T. and Z.W. All authors have read and agreed to the published version of the manuscript.

Funding: This work is supported by National Natural Science Foundation of China (No.: 51876099).

Institutional Review Board Statement: Not applicable.

Informed Consent Statement: Not applicable.

Data Availability Statement: Not applicable.

Acknowledgments: The author sincerely thanks the project support: "Research on the Safe and Stable Operation of the Datongxia Large Kaplan Tubrbine Project" from Guangxi Datengxia Gorge Water Conservancy Development Co., Ltd.

Conflicts of Interest: The authors declare no conflict of interest.

Abbreviations

The following abbreviations are used in this manuscript:

CFD Computational fluid dynamics

References

1. Cui, R.G.; Guo, J.; Cheng, L.H. Status and Trends Analysis of Global Clean Energies. *Acta Geosci. Sin.* **2021**, *42*, 179–186.
2. Ma, W.S. *Simulation of the Whole Passage in Prototype Turbine and Analysis of Precision in Calculation*; China Agricultural University: Beijing, China, 2005.
3. Estevez, E.E. *Comportament Dinàmic de Màquines Hidràuliques*; Universitat Politècnica de Catalunya: Barcelona, Spain, 2004.
4. Wu, S.F.; Wu, Y.L.; Liu, C.H. The characteristics prediction and the operating comprehensive performance curve drawing of Kaplan turbine. *J. Hydroelectr. Eng.* **2008**, *27*, 121–125.
5. Liu, X.; Luo, Y.Y.; Wang, Z.W. A review on fatigue damage mechanism in hydro turbines. *Renew. Sustain. Energy Rev.*. **2016**,*54*,1–14. [CrossRef]
6. Zhou, L.J.; Wang, Z.W.; Xiao, R.F. Analysis of dynamic stresses in Kaplan turbine blades. *Eng. Comput*. **2007**, *24*, 753–762. [CrossRef]
7. Liu, S.; Li, S.; Wu, Y. Pressure fluctuation prediction of a model Kaplan turbine by unsteady turbulent flow simulation. *Fluids Eng.*. **2009**, *131*, 101102. [CrossRef]
8. Rodriguez, C.G.; Egusquiza, E.; Santos, I.F. Frequencies in the vibration induced by the rotor stator interaction in a centrifugal pump turbine. *Fluids Eng*. **2007**, *129*, 1428–1435. [CrossRef]
9. Jonsson, P.P.; Mulu, B.G.; Cervantes, M.J. Experimental investigation of a Kaplan draft tube-Part II: Off-design conditions. *Energy* **2012**, *94*, 71–83. [CrossRef]
10. Amiri, K.; Mulu, B.; Raisee, M. Load variation effects on the pressure fluctuations exerted on a Kaplan turbine runner. *IOP Conf. Ser. Earth Environ*. **2014**, *22*, 32005. [CrossRef]
11. Motycak, L.; Skotak, A.; Kupcik, R. Kaplan turbine tip vortex cavitation-analysis and prevention. *IOP Conf. Ser. Earth Environ. Sci.* **2012**, *15*, 32060. [CrossRef]

12. Kumar, P.; Saini, R.P; Cheng, L.H. Study of cavitation in hydro turbines—A review. *Renew. Sustain. Energy Rev.* **2010**, *14*, 374–383. [CrossRef]
13. Wang, Z.W.; Luo, Y.Y.; Zhou, L.J. Computation of dynamic stresses in piston rods caused by unsteady hydraulic loads. *Eng. Fail.* **2008**, *15*, 28–37. [CrossRef]
14. Urquiza, J.; Garcia, J.C.; Gonzalez, J.G. Failure analysis of a hydraulic Kaplan turbine shaft. *Eng. Fail.* **2014**, *41*, 108–117. [CrossRef]
15. Luo, Y.Y.; Wang, Z.W.; Zeng, J. Fatigue of piston rod caused by unsteady, unbalanced, unsynchronized blade torques in a Kaplan turbine. *Eng. Fail.* **2010**, *17*, 192–199. [CrossRef]
16. Liu, S.; Shao, J.; Wu, S. Numerical simulation of pressure fluctuation in Kaplan turbine. *Sci. China Ser. E-Technol. Sci.* **2008**, *51*, 1137–1148. [CrossRef]
17. Wu, Y.; Liu, S.; Dou, H. Numerical prediction and similarity study of pressure fluctuation in a prototype Kaplan turbine and the model turbine. *Comput. Fluids* **2012**, *56*, 128–142. [CrossRef]
18. Zhang, Y.; Chen, T.; Li, Z. Experimental Study of Load Variations on Pressure Fluctuations in a Prototype Reversible Pump Turbine in Generating Mode. *J. Fluids Eng. Trans. ASME*. **2017**, *139*, 074501. [CrossRef]
19. Zhou, L.J. *Flow Field Simulation and Property Prediction for Hydraulic Turbine Runner*; China Agricultural University: Beijing, China, 1999.
20. Ruprecht, A.; Heitele, M.; Helmrich, T. *Numerical Simulation of a Complete Francis Turbine including Unsteady Rotor/Stator Interactions*; IAHR: Madrid, Spain, 2000.
21. Li, G.F.; Lu, C. Experiment on pressure fluctuation of Kaplan turbine with low specific speed. *J. Drain. Irrig. Mach.* **2017**, *35*, 869–873.
22. Gao, M. Experiment on pressure fluctuation of Kaplan turbine with low specific speed. *New Technol. New Prod. China* **2018**, *13*, 61–62.
23. Zhu, G.J.; Li, K.; Feng, J.J. Influence of cavitation on pressure fluctuation of draft tube and runner vibration of Kaplan turbine. *Trans. Chin. Soc. Agric. Eng.* **2021**, *37*, 40–49.
24. Kim, H.; Rakibuzzaman, M.; Kim, K. Flow and Fast Fourier Transform Analyses for Tip Clearance Effect in an Operating Kaplan Turbine. *Energies* **2019**, *12*, 264. [CrossRef]
25. Wu, Y.; Feng, J.J.; Wu, G.K. Study on effects of hub clearance flow on Kaplan turbine performance. *J. Hydroelectr. Eng.*. **2014**, *33*, 185–190.
26. Petit, O.; Nilsson, H.; Vu, T. The flow in the U9 Kaplan turbine–preliminary and planned simulation using AND openfoam. In Proceedings of 24th IAHR Symposium on Hydraulic Machinery and Systems, Foz Do Iguassu, Brazil, 27–31 October 2008.
27. Vu, T.C.; Shyy, W. Performance Prediction of Viscous Flow Analysis for Francis Turbine Runner. *J. Fluids Eng.* **1994**, *116*, 116–120 [CrossRef]
28. Vu, T.C.; Heon, K.; Shyy, W. An Integrated CFD Tool for Hydraulic Turbine Efficiency Prediction. In Proceedings of the 5th International Symposium of Refined Flow Modeling and Turbulence Measurements, Paris, France, 7–10 September 1993.
29. Gehrer, A.; Schmidl, R.; Sadnik, D. Kaplan turbine runner optimization by numerical flow simulation (CFD) and an evolutionary algorithm. In Proceedings of 23rd IAHR Symposium on Hydraulic Machinery and Systems, Yokohama, Japan, 17–21 October 2006.
30. Shingai, K.; Katayama, K.; Shimmei, K. Optimization of axial turbine runner blade using a simulated annealing algorithm. In Proceedings of 23rd IAHR Symposium on Hydraulic Machinery and Systems, Yokohama, Japan, 17–21 October 2006.
31. Escaler, X.; Egusquiza, E.; Farhat, M. Detection of cavitation in hydraulic turbines. *Mech. Syst. Signal Process.* **2006**, *20*, 983–1007. [CrossRef]
32. Thiery, F.; Gustavsson, R.; Aidanpää, J. Dynamics of a misaligned Kaplan turbine with blade-to-stator contacts. *Int. J. Mech. Sci.* **2015**, *99*, 251–261. [CrossRef]
33. Zhou, X.; Shi, C.; Miyagawa, K. Investigation of Pressure Fluctuation and Pulsating Hydraulic Axial Thrust in Francis Turbines. *Energies* **2020**, *13*, 17347. [CrossRef]
34. Luo, Y.Y. *Study on Flow Induced Structure Dynamic Characteristics for Kaplan Turbine*; Tsinghua University: Beijing, China, 2010.
35. Yakhot, V.; Orszag, S.A. Renormalization group analysis of turbulence–I: Basic Theory. *Sci. Comput.* **1986**, *1*, 3–51. [CrossRef]
36. Speziale, C.G.; Thangam, S. Analysis of a RNG based turbulence model for separated flows Int. *Eng. Sci.* **1992**, *30*, 1379–1388.
37. Menter, F.R. *Zonal Two-Equation $k-\omega$ Turbulence Model for Aerodynamic Flows*; AIAA Paper; American Institute of Aeronautics and Astronautics: Reston, VA, USA, 1993
38. Menter, F.R. Two-equation eddy-viscosity turbulence models for engineering applications. *AIAA J.* **1994**, *32*, 1598–1605. [CrossRef]

Disclaimer/Publisher's Note: The statements, opinions and data contained in all publications are solely those of the individual author(s) and contributor(s) and not of MDPI and/or the editor(s). MDPI and/or the editor(s) disclaim responsibility for any injury to people or property resulting from any ideas, methods, instructions or products referred to in the content.